J Comput Aided Mol Des (2012) 26:1327–1342
DOI 10.1007/s10822-012-9617-3

Computational insights into the selectivity mechanism of APP-IP over matrix metalloproteinases

Lingling Geng · Jian Gao · Wei Cui · Yancheng Tang · Mingjuan Ji · Bozhen Chen

Received: 16 July 2012 / Accepted: 6 November 2012 / Published online: 9 December 2012

Abstract In this work, selectivity mechanism of APP-IP inhibitor (β-amyloid precursor protein-derived inhibitory peptide) over matrix metalloproteinases (MMPs including MMP-2, MMP-7, MMP-9 and MMP-14) was investigated by molecular modeling methods. Among MMPs, MMP-2 is the most favorable one for APP-IP interacting based on our calculations. The predicted binding affinities can give a good explanation of the activity difference of inhibitor APP-IP. In Comparison with MMP-2/APP-IP complex, the side chain of $Tyr214^{MMP\text{-}7}$ makes the binding pocket so shallow that the whole side chain of $Tyr3^{APP\text{-}IP}$ can not be fully embraced, thus unfavorable for the N-terminal of APP-IP binding to MMP-7. The poor selectivity of APP-IP toward MMP-9 is mainly related with the decrease of interaction between the APP-IP C-terminal and MMP-9 due to the bulky side chains of Pro193 and Gln199, which is in agreement with experiment. The mutations at residues P193A and Q199G of MMP-9 alternate the binding pattern of the C-terminal of APP-IP by forming two new hydrogen bonds and hydrophobic interactions with MMP-9. The mutants favor the binding affinity of MMP-9 largely. For MMP-14/APP-IP, the large steric effect of $Phe204^{MMP\text{-}14}$ and the weak contributions of the polar residues $Asn231^{MMP\text{-}14}$ and $Thr190^{MMP\text{-}14}$ could explain why MMP-14 is non-selective for APP-IP interacting. Here, the molecular modeling methods were successfully employed to explore the selective inhibitor of MMPs, and our work gives valuable information for future rational design of selective peptide inhibitors toward individual MMP.

Keywords Molecular dynamics · Matrix metalloproteinase · MMP-2-selective inhibitor APP-IP · MM/GBSA

Introduction

Matrix metalloproteinases (MMPs), the matrix-degrading enzymes, represent a larger family of zinc-dependent endopeptidases that have evolved to digest specific extracellular matrix (ECM) components. The timely breakdown of ECM is essential for embryonic development, morphogenesis, tissue resorption and remodeling under both physiological and pathological conditions such as tumor invasion [1–4]. MMPs can be subdivided in different groups such as collagenases (MMP-1, MMP-8, MMP-13), gelatinases (MMP-2, MMP-9), matrilysins (MMP-7, MMP-26), stromelysins (MMP-3, MMP-10, MMP-11), and the membrane-type MMPs (MT-MMPs, such as MT1-MMP also named MMP-14). Among those MMPs, MMP-2 and MMP-9 play an important role in metastasis through interaction with gelatinases's main substrates type IV collagen, which is the major cause of morbidity and death for cancer patients [5–7]. The primary structure of MMPs comprises several domain motifs, the three common

Electronic supplementary material The online version of this article (doi:10.1007/s10822-012-9617-3) contains supplementary material, which is available to authorized users.

L. Geng · J. Gao · W. Cui · M. Ji (✉) · B. Chen (✉)
School of Chemistry and Chemical Engineering, Graduate University of Chinese Academy of Sciences, Beijing 100049, People's Republic of China
e-mail: jmj@gucas.ac.cn

B. Chen
e-mail: bozhenchen@hotmail.com

Y. Tang
School of Basic Medical Sciences, Peking University Health Science Center, Beijing 100191, People's Republic of China

domains of which are the pro-peptide, the catalytic domain, and the C-terminal haemopexin-like domain linked to the catalytic domain by a flexible hinge region [8–11].

Most of the newly synthesized MMPs are secreted as pro-MMP, which is known as an inactive zymogen and activated by serine proteases or some activated MMPs. Tissue inhibitors of matrix metalloproteinases (TIMPs) can regulate the activities of activated MMPs in vovo, and have broad specificity against MMPs. Therefore, the balance between TIMPs and MMPs is important for the remodeling of eventual ECM in the tissue. So far, four inhibitor members of TIMP family have been identified and designated as TIMP-1, -2, -3, and -4 in humans, and they showed inhibition effect toward to almost all MMPs [12–15]. Many synthetic MMP inhibitors have also been reported such as the hydroxamate-based inhibitors. Nevertheless, they are not specific inhibitors of individual MMPs [16–19]. The relatively high sequence homology (>40 %) of MMPs determines the close similarity in the overall three-dimensional structure, thus it is a nontrivial task to design a selective MMP inhibitor.

In 2003, the Shouichi Higashi's group discovered that APP (β-amyloid precursor protein)-derived inhibitory peptide (APP-IP), unlike other synthetic or physiological inhibitors, is a specific inhibitor selectively against gelatinase A (MMP-2). Moreover, the MMP-2-selective inhibitor APP-IP is a synthetic decapeptide containing the ISYGNDALMP sequence corresponding to residues 586–595 of APP_{770} [20]. In addition, there was a big gap between the inhibitory activities of APP-IP toward MMP-2 ($IC_{50} = 30$ nM), MT1-MMP (MMP-14) ($IC_{50} = 2$ μM) and gelatinase B (MMP-9), matrilysin (MMP-7), stromelysin (MMP-3) ($IC_{50} > 10$ μM). In 2008, Shouichi Higashi and his partners [21] further investigated the selective inhibition of APP-IP by constructing various chimeric mutants of MMPs. In 2011, they obtained the crystal structure of the MMP-2 mutant (E108K, Q110V, E121A) with APP-IP [22]. Their researches indicated that residues Tyr3, Asp6 and Leu8 of APP-IP have relatively large contribution in its binding affinity to MMP-2, and residues Ala87, Gly93, Tyr144 and Thr145 of MMP-2 are associated with the selectivity in comparison with the corresponding residues of MMP-7 and MMP-9 [21, 22]. However, the detailed molecular mechanisms about how APP-IP interacts with MMPs except MMP-2 and why it is non-selective interacting with other MMPs are still needed to be clarified.

In the present paper, to elucidate the mechanism of the selective inhibition of APP-IP, we systemically investigated the interaction mechanisms between APP-IP and MMPs by using molecular dynamics (MD) simulations and molecular mechanics/generalized born surface area (MM/GBSA) binding free energy calculation and MM/GBSA free energy decomposition methods [23–26]. Based on the calculations, we will uncover the selectivity mechanism of APP-IP toward MMP-2, MMP-7, MMP-9 and MMP-14.

Materials and methods

Primary sequence alignment and the initial structure

Primary sequences of MMP-2, MMP-7, MMP-9 and MMP-14 were aligned by using ClustalW program available on the web of EMBnet [27].

The wild type (WT) model of MMP-2/APP-IP complex was constructed based on the crystal structure of MMP-2 (E108K, Q110V, E121A)/APP-IP complex (PDB entry: 3AYU), by re-mutating the targeting residues into the desired amino acids [22, 28]. The models of MMP-7/APP-IP, MMP-9/APP-IP and MMP-14/APP-IP complexes were constructed based on the crystal structure of MMP-7/hydroxamate inhibitor (PDB entry: 1MMQ), MMP-9/hydroxamate inhibitor (PDB entry: 1GKC), MMP-14/TIMP-2 inhibitor (PDB entry: 1BUV) and MMP-2 (E108K, Q110V, E121A)/APP-IP complexes. All of the above crystal structures were retrieved from the RCSB Brookhaven protein data bank (PDB) [22, 28–31]. In order to construct the MMP-7/APP-IP complex, the crystal structure of MMP-7/hydroxamate inhibitor complex was superimposed onto the structure of MMP-2/APP-IP complex, and the APP-IP was extracted and merged into the MMP-7/hydroxamate inhibitor complex in SYBYL7.1. Then, hydroxamate inhibitor was deleted and the MMP-7/APP-IP complex was obtained. The same methods were conducted on the MMP-9/APP-IP and MMP-14/APP-IP complexes to get their respective model. The two mutants $MMP\text{-}9^{P193A}$/APP-IP and $MMP\text{-}9^{P193A,\ Q199G}$/APP-IP complexes were mutated from MMP-9/APP-IP complex. In the MMP-9/APP-IP and its two mutant systems, the N-terminal two residues Phe110 and Glu111 in MMP-9 were removed.

For protonation states of residues, histidine was assigned HIE (histidine with hydrogen on the epsilon nitrogen) state in default, while histidines around ions Zn^{2+} or Ca^{2+} in MMPs proteins were changed from HIE to HID (histidine with hydrogen on the delta nitrogen) state according to the interacting type between ions and histidine. Other alkaline and acidic amino acids were also charged. Each constructed structure was immersed in a truncated octahedron box with TIP3P [32] water molecules, and the missing hydrogen atoms of each model were added via the *tleap* program, then the complexes were minimized by the *sander* program in AMBER9.0 [33] via three steps: firstly, the water molecules and the merged residues were minimized by restraining the protein (10,000 cycles of steepest descent and 5,000 cycles of conjugate gradient minimizations); secondly, the amino acid backbone atoms (N, CA, C, O)

and the ions were restrained and the rest side chains were minimized (10,000 cycles of steepest descent and 5,000 cycles of conjugate gradient minimizations); thirdly, the whole system was minimized without any restraint (10,000 cycles of steepest descent and 5,000 cycles of conjugate gradient minimizations). After minimization, the water molecules were deleted, and the final structure of each model was saved by SYBYL7.1.

MD simulations

The AMBER03 force field was used to establish the potentials of the proteins in the following molecular mechanics (MM) minimizations and MD simulations [34]. The force field parameter of Ca^{2+} was downloaded from the AMBER parameter database; the force field parameter of Zn^{2+} used the previously derived ones [35]. The whole system was solvated in a truncated octahedron box filled with 8 Å TIP3P water molecules, with a minimum solute-wall distance of 12 Å [32]. Then, counter-ions Na^+ or Cl^- were placed on the grids with the largest negative or positive Coulombic potentials around the protein.

Before the MD simulations, the same minimization method was used to minimize the complexes as in the constructing initial structure part. The SHAKE procedure was applied, and the time step was set to 2.0 fs [36]. Particle Mesh Ewald (PME) was employed to deal with the long-range electrostatic interactions in the MD simulations [37]. Followed by minimization, the entire systems were gradually heated in the canonical ensemble from 0 to 310 K via seven steps in the NVT. Finally, 12 ns MD simulations were carried out under the constant temperature of 310 K. During the sampling process, the coordinates were saved every 0.2 ps, and the conformations generated from the simulations were used for further binding free energy calculations and decomposition analysis.

Binding free energy calculations

The binding free energy of each system was calculated using MM/GBSA technique according to the following equation [38].

$$\begin{aligned}\Delta G_{\text{bind}} &= G_{\text{complex}} - G_{\text{protein}} - G_{\text{ligand}} \\ &= \Delta E_{\text{MM}} + \Delta G_{\text{GB}} + \Delta G_{\text{SA}} - T\Delta S \\ &= \Delta E_{\text{vdW}} + \Delta E_{\text{ele}} + \Delta G_{\text{GB}} + \Delta G_{\text{SA}} - T\Delta S \qquad (1)\end{aligned}$$

where ΔE_{MM} is the interaction energy between protein and ligand in gas-phase, including the parts: the van der Waals energies (ΔE_{vdW}) and the electrostatic (ΔE_{ele}); ΔG_{GB} and ΔG_{SA} are the relative polar and nonpolar contributions to desolvation free energy, respectively, and $-T\Delta S$ represents the conformational entropic contribution at temperature T. In this study, the polar solvation free energy was calculated by the generalized born (GB) model [39]. In the GB calculations, the solvent and the solute dielectric constants were set to 80 and 4, respectively. The nonpolar solvation term was estimated based on the solvent accessible surface area (SASA) model by the LCPO method with a solvent-probe radius of 1.4 Å: $\Delta G_{\text{SA}} = 0.0072 \times \Delta\text{SASA}$ [40]. The binding free energy of each system was calculated based on 1,000 snapshots from 8 to 12 ns MD simulation trajectories of each complex by using the *mm_pbsa* program in AMBER9.0 [33]. The conformational entropy (translation, rotation and vibration) upon the ligand binding ($-T\Delta S$) was calculated using normal-mode analysis via the *nmode* program in AMBER9.0 [33]. Due to the high computational demand of this approach, only 50 snapshots evenly extracted from the last 4 ns were used to estimate the entropic contribution.

Free energy decomposition analysis

To analyze the key residues in the interaction between MMPs and APP-IP the MM/GBSA free energy decomposition process was applied by the *mm_pbsa* program in AMBER9.0 [41]. The essential idea of binding free energy decomposition was to decompose the energy contribution of each residue from the association of the receptor with the ligand into four parts: van der Waals contribution (ΔE_{vdW}), electrostatic contribution (ΔE_{ele}), polar part, and nonpolar of solvation ($\Delta G_{\text{GB}} + \Delta G_{\text{SA}}$) contribution. The polar contribution of desolvation free energy (ΔG_{GB}) was calculated using the generalized Born (GB) approximation model developed by Onufriev et al. [42], and the nonpolar solvation contribution (ΔG_{SA}) part was computed based on the SASA determined with the ICOSA method [40]. All the energy components were calculated using 1,000 snapshots extracted from the MD trajectory from 8 to 12 ns. The molecular surface and cartoon figures were generated by PyMOL [43].

Results and discussion

Primary sequence alignment and stability of system simulations

Primary sequence alignment

Residue sequences of MMP-2, MMP-7, MMP-9 and MMP-14 were aligned to get a clear representation of the primary structure by using ClustalW program available on the web of EMBnet, and the results were plotted in Fig. 1. It is clear that MMP-2, MMP-7, MMP-9 and MMP-14 have a high

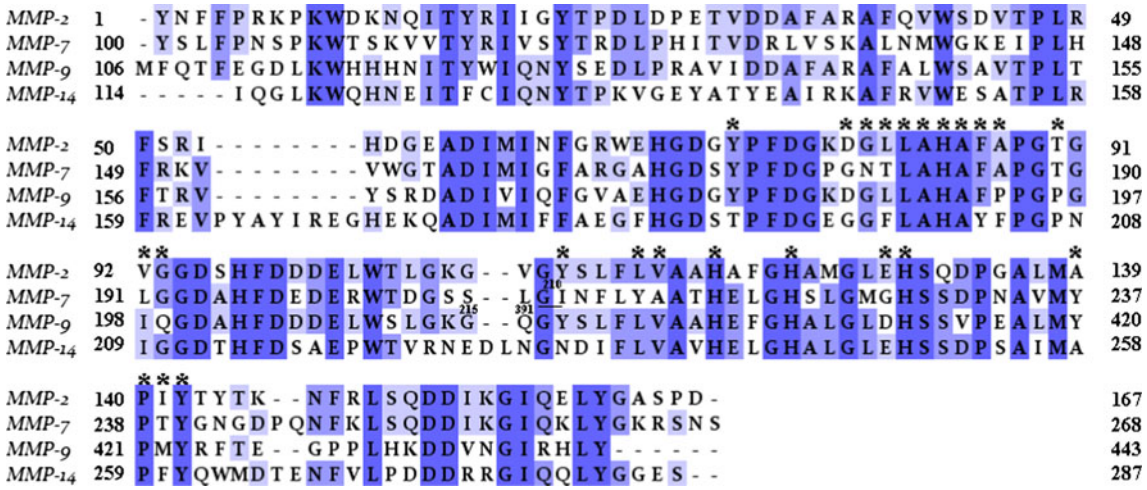

Fig. 1 The plot of aligning residue sequences of MMP-2 (E108K, Q110V, E121A), MMP-7, MMP-9 and MMP-14. (The number 210 in crystal structure of MMP-7 has two residues Gly210 and Ile210, respectively; Numbers between 215 and 391 in crystal structure of MMP-9 have no residues. The important residues in MMP-2 around of APP-IP within 5 Å range are labeled with *asterisks*. Various shades of *blue* represent the different levels of amino acid homology)

level of homology in the primary structure. But some key residues available for APP-IP binding are different in their amino acid volume or property, such as residues $Tyr73^{MMP\text{-}2}$, $Ala87^{MMP\text{-}2}$, $Gly93^{MMP\text{-}2}$ and $Leu116^{MMP\text{-}2}$ compared with the corresponding residues in other MMPs.

Stability of system simulations

Here, we performed classical MD simulations on MMP-2/APP-P, MMP-7/APP-IP, MMP-9/APP-IP, $MMP\text{-}9^{P193A}$/APP-IP, $MMP\text{-}9^{P193A,\ Q199G}$/APP-IP and MMP-14/APP-IP complexes to predict their binding mode, and explore the key residues associated with the inhibitor selectivity. To obtain the equilibrated and stable systems, and to ensure the rationality of sampling strategy, the 12 ns MD simulations on the six complexes were carried out. To explore the stability of all complexes, the root-mean-square-deviation (RMSD) of all the protein backbone atoms were calculated based on the initial structure and the results were plotted in Fig. 2. It shows that the RMSD values of the backbone atoms in all complex increase sharply within 3,000 ps and then remain stable to the end. The RMSD value of MMP-7/APP-IP system has a fluctuation at 8,000 ps and then keeps smooth to the end. As shown in Fig. 2, the MMP-2/APP-IP system is more stable than the other systems during the whole MD simulation, and the average value of RMSD is 1.18 Å. As for the other five systems, MMP-7/APP-IP, MMP-14/APP-IP, MMP-9/APP-IP, $MMP\text{-}9^{P193A}$/APP-IP and $MMP\text{-}9^{P193A,Q199G}$/APP-IP, the RMSD fluctuates largely but still within the acceptable scale with average values of 1.41, 2.00, 1.31, 1.64 and 1.53 Å, respectively. The RMSD values of the backbone atoms of APP-IP also remain stable after the 8 ns MD simulation in all complexes (see supporting information). The results suggest that it is reasonable and reliable to do the following MM/GBSA binding free energy calculations and MM/GBSA free energy decomposition analyses based on the snapshots extracted from 8 to 12 ns.

Binding free energy calculated by MM/GBSA

After the 12 ns MD simulations on MMP-2/APP-P, MMP-7/APP-IP, MMP-9/APP-IP, $MMP\text{-}9^{P193A}$/APP-IP, $MMP\text{-}9^{P193A,\ Q199G}$/APP-IP and MMP-14/APP-IP complexes, MM/GBSA method was applied to calculate the binding affinity between MMPs and APP-IP.

The predicted binding free energy and the energy components, together with experimentally derived IC_{50} values of the six systems are listed in Table 1. As shown in Table 1, the calculated binding affinity of MMP-2/APP-IP complex (−79.65 kcal/mol) is stronger than that of the MMP-7/APP-IP (−48.44 kcal/mol), MMP-9/APP-IP (−36.56 kcal/mol) and MMP-14/APP-IP (−46.45 kcal/mol) complexes, which indicates that MMP-2 is more favorable for APP-IP binding. In addition, compared to MMP-9/APP-IP complex, the single mutant $MMP\text{-}9^{P193A}$/APP-IP complex (−40.78 kcal/mol) increases the binding affinity by about 4 kcal/mol, and the double mutant $MMP\text{-}9^{P193A,\ Q199G}$/APP-IP complex (−52.62 kcal/mol) highly increases the binding affinity by about 16 kcal/mol. However, compared with MMP-2, MMP-9 and its two mutants still show lower contributions for APP-IP binding. It can be seen that the calculated binding free energies for the six systems are consistent with the corresponding experimental values [20, 21]. According to the IC_{50}, the experimental binding free energy was calculated by $\Delta G \approx -RT \ln IC_{50}$,

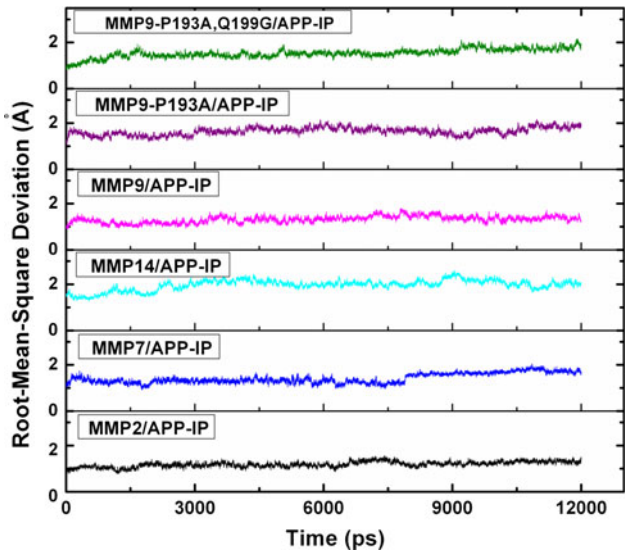

Fig. 2 The root-mean-square deviation (rmsd) of the backbone atoms (CA, N, C) of the six complexes relative to the starting structure

and the square of correlation coefficient R^2 between the calculated and experimental binding free energy is 0.87, which also indicates that the predicted results are reliable.

Furthermore, the four individual energy components (ΔE_{ele}, ΔE_{vdw}, ΔG_{GB}, ΔG_{SA}) are compared carefully in order to get a better view on which energy term has more impact on the binding affinities. From data shown in Table 1, it is clear that the van der Waals (ΔE_{vdw}) contribution is the main component in the total binding free energy and plays an essential role for the binding affinity in every complex (−101.08, −67.52, −63.72, −69.55, −78.24 and −72.19 kcal/mol for MMP-2/APP-IP, MMP-7/APP-IP, MMP-9/APP-IP, MMP-9^{P193A}/APP-IP, MMP-$9^{P193A,Q199G}$/APP-IP, and MMP-14/APP-IP, respectively), following the electrostatic (ΔE_{ele}) contribution. The ΔE_{ele} contributions of MMP-2/APP-IP and MMP-7/APP-IP are stronger than those of the other four complexes. However, the net electrostatic contributions ($\Delta E_{ele} + \Delta G_{GB}$) of the six complexes are unfavorable for the binding between MMPs and APP-IP (6.05, −1.36, 3.71, 4.73, 3.96 and 3.72 kcal/mol for the six systems, respectively). The nonpolar desolvation energies (ΔG_{SA}) of these six systems are similar to each other (−12.68, −9.88, −9.65, −10.62, −11.66 and −10.54 kcal/mol for MMP-2/APP-IP, MMP-7/APP-IP, MMP-9/APP-IP, MMP-9^{P193A}/APP-IP, MMP-$9^{P193A,Q199G}$/APP-IP, and MMP-14/APP-IP, respectively). The six complexes have similar conformational entropic contributions ($-T\Delta S$) and the differences are within 6 kcal/mol (see Table 1). Therefore, the van der Waals contribution is more crucial for APP-IP interacting with MMPs, and for distinguishing the binding affinities among these six complexes.

Selectivity mechanism of APP-IP toward MMPs

To further understand the detailed interaction of MMPs/APP-IP complexes, and to find the main residues in MMPs affecting the inhibitor's selectivity, MM/GBSA method was applied to decompose the total binding free energies into residue–residue pairs, which would provide more useful information of each residue's contribution. The comparisons of the key residues of MMPs and APP-IP for the MMP-2/APP-IP, MMP-7/APP-IP, MMP-9/APP-IP and MMP-14/APP-IP complexes are shown in Fig. 3. The binding modes of these complexes with the key residues labeled in the binding pocket are plotted in Fig. 4.

Binding mode of APP-IP in the different complexes

In order to find out the reasons of the different binding affinities in the four complexes, it is better to start with an investigation of each residue's contribution in APP-IP.

The comparison of the conformation of APP-IP based on the superposed complexes is conducted to clearly observe the different binding modes of APP-IP and MMPs (Fig. 4a). Apparently, APP-IP^{MMP-2} entering into the pocket of MMP-2 is deeper than APP-IP^{MMP-7}, APP-IP^{MMP-9} and APP-IP^{MMP-14}. The N-terminal of APP-IP^{MMP-7} and

Table 1 Binding free energies and individual energy terms of MMPs/APP-IP calculated by MM/GBSA (kcal/mol)

MMPs/APP-IP complexes	ΔE_{ele}	ΔE_{vdw}	ΔG_{GB}	ΔG_{SA}	$-T\Delta S$	ΔG_{pred}	IC_{50} [20, 21]
MMP-2/APP-IP	−64.94 ± 7.24	−101.08 ± 4.38	70.99 ± 6.44	−12.68 ± 0.45	28.06 ± 4.40	−79.65 ± 4.62	30 nM
MMP-7/APP-IP	−71.22 ± 3.24	−67.52 ± 4.26	69.86 ± 3.05	−9.88 ± 0.40	30.32 ± 4.17	−48.44 ± 4.16	20 μM
MMP-9/APP-IP	−36.41 ± 4.85	−63.72 ± 5.54	40.12 ± 4.61	−9.65 ± 0.67	33.1 ± 3.50	−36.56 ± 5.57	250 μM
MMP-9^{P193A}/APP-IP	−32.47 ± 3.32	−69.55 ± 4.15	37.20 ± 2.92	−10.62 ± 0.42	34.65 ± 4.28	−40.78 ± 3.98	28 μM
MMP-$9^{P193A,\ Q199G}$/APP-IP	−38.95 ± 3.59	−78.24 ± 4.67	42.91 ± 3.44	−11.66 ± 0.30	33.32 ± 5.40	−52.62 ± 4.54	1.3 μM
MMP-14/APP-IP	−34.12 ± 3.36	−72.19 ± 3.92	37.84 ± 2.87	−10.54 ± 0.29	32.56 ± 4.84	−46.45 ± 4.11	2 μM

ΔE_{ele}, electrostatic contribution; ΔE_{vdw}, van der Waals contribution; ΔG_{GB}, the polar contribution of desolvation; ΔG_{SA}, nonpolar contribution of desolvation; $-T\Delta S$, the conformational entropy at temperature T

C-terminal of APP-IP^{MMP-9} are unfavorable for their respective receptor binding. After the mutations on MMP-9, the C-terminals of APP-IP$^{MMP-9–P193A}$ and APP-IP$^{MMP-9–P193A,\ Q199G}$ move closer to the receptor protein MMP-9. Moreover, for MMP-14/APP-IP, it seems that both N and C terminals of APP-IP are similar to that in MMP2/APP-IP complex.

The key residues of APP-IP, which are responsible for the binding affinity differences among the four complexes,

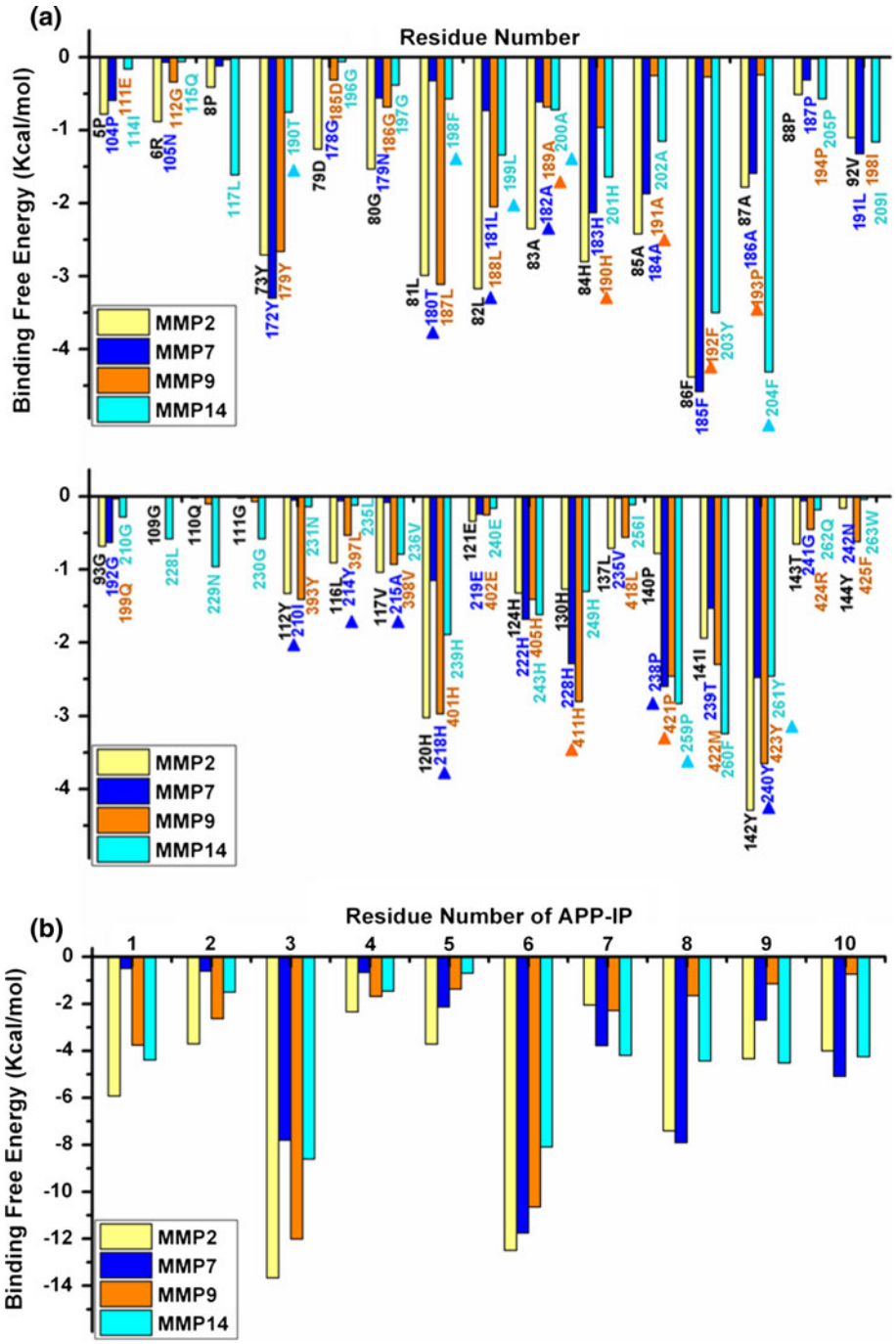

Fig. 3 The comparisons of key residues of MMPs (**a**) and APP-IP (**b**) for MMP-2/APP-IP, MMP-7/APP-IP, MMP-9/APP-IP and MMP-14/APP-IP systems. Compared with MMP-2, main distinct residues of MMP-7, MMP-9 and MMP-14 are labeled with *triangle* symbol

Fig. 4 Binding modes of MMPs/APP-IP complexes with key residues in the binding pockets. The MMPs are shown as cartoon (in *yellow*), the side chains of residues in MMPs are shown as a stick drawing (in *cyan*), the residues of APP-IP shown as sticks (in *pink*), and the zinc ions are shown as spheres (in *green*). **a** the comparison of the different binding modes of APP-IP and MMPs based on the superimposed complexes. It is the N-terminal to C-terminal direction from the left to the right. **b** MMP-2/APP-IP complex. **c** MMP-7/APP-IP complex. **d** MMP-9/APP-IP complex. **e** MMP-9^{P193A}/APP-IP complex. **f** MMP-9$^{P193A,\ Q199G}$/APP-IP complex. **g** MMP-14/APP-IP complex ►

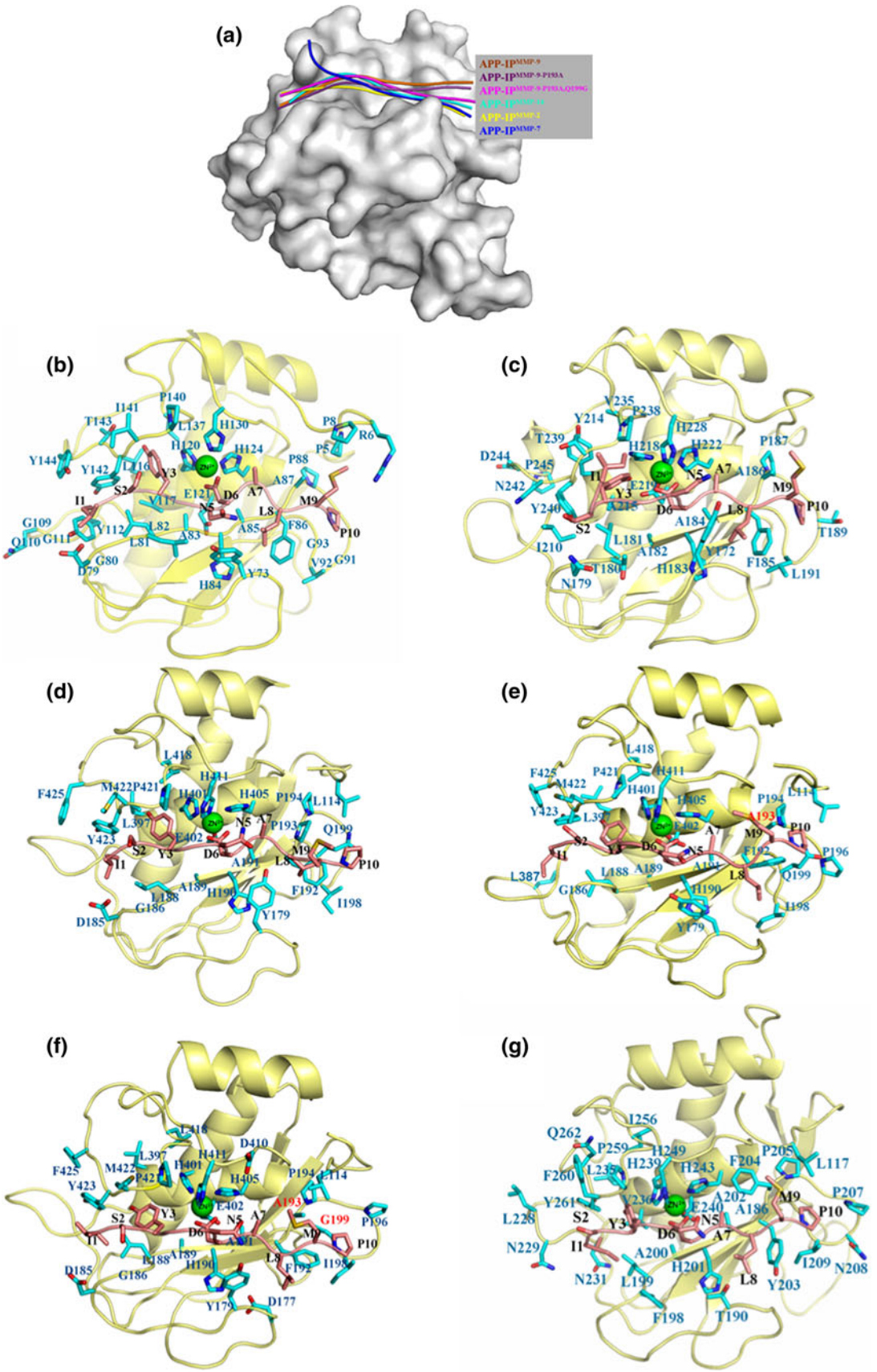
(a)
APP-IP^MMP-9
APP-IP^MMP-9-P193A
APP-IP^MMP-9-P193A,Q199G
APP-IP^MMP-1
APP-IP^MMP-7
(b)
(c)
(d)
(e)
(f)
(g)

can be obtained by free energy decomposition analyses. As shown in Fig. 3b, Tyr3^{APP-IP}, Asp6^{APP-IP} and Leu8^{APP-IP} in MMP-2/APP-IP are the main residues responsible for the free energy contribution, which is consistent with the experimental data [22]. Compared with MMP-2/APP-IP complex, it can be seen that the binding affinity of the N-terminal of APP-IP with residues Ile1 (−0.49 kcal/mol), Ser2 (−0.61 kcal/mol) and Tyr3 (−7.80 kcal/mol) in MMP-7/APP-IP complex is much weaker than that in MMP-2/APP-IP complex (−5.92, −3.70, −13.66 kcal/mol), which affects the binding affinities of MMP-7/APP-IP complex. As for MMP-9/APP-IP complex, it can be found that the binding affinity of the C-terminal of APP-IP with residues Leu8 (−1.65 kcal/mol), Met9 (−1.14 kcal/mol), Pro10 (−0.74 kcal/mol) is much weaker than that of MMP-2/APP-IP complex (−7.4, −4.33, and −4.00 kcal/mol). The distinct difference between MMP-14/APP-IP and MMP-2/APP-IP complexes mainly locates at residues Tyr3 (−8.61, −13.66 kcal/mol), Asn5 (−0.69, −3.71 kcal/mol), Asp6 (−8.09, −12.49 kcal/mol) and Leu8 (−4.43, −7.40 kcal/mol).

The results of the free energy decomposition analyses of APP-IP indicate that MMP-2 is the most favorable one for the inhibitor binding. In the following section, we will describe and discuss the detail interaction mechanisms between APP-IP and MMPs.

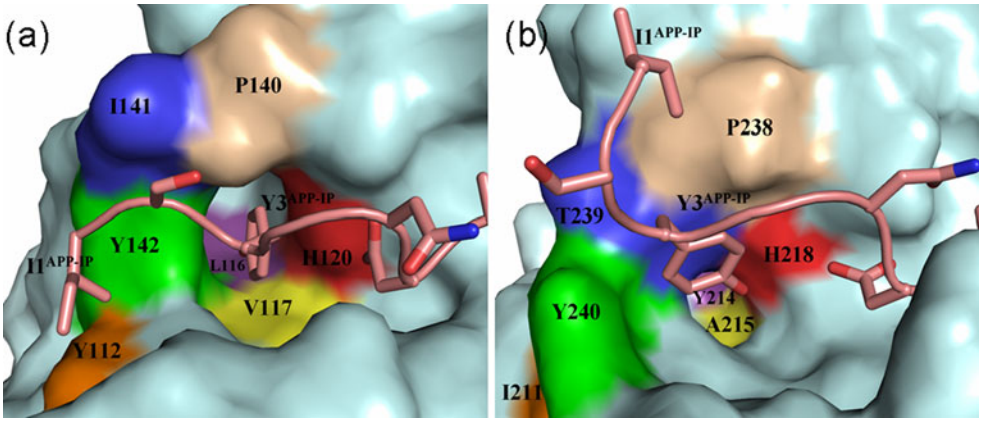

Fig. 5 The binding pockets of the N-terminal of APP-IP, which is shown in surface mode labeled with key residues of MMP-2 (**a**) and MMP-7 (**b**)

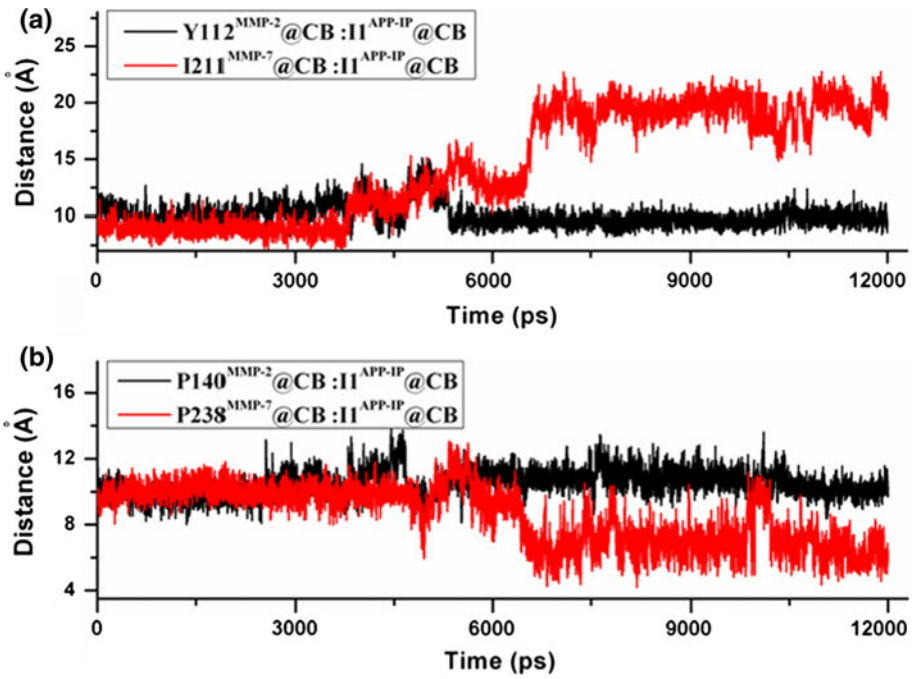

Fig. 6 Distance between atom CB (Ile1^{APP-IP}) and atom CB (Ile211^{MMP-7}) (**a**), between atom CB (Ile1^{APP-IP}) and atom CB (Pro238^{MMP-7}) (**b**) in MMP-7/APP-IP complex as well as the corresponding distance in MMP-2/APP-IP complex during 12 ns MD simulation

MMP-7/APP-IP system

The key residues of MMP-7/APP-IP complex are shown in Fig. 4c. Residues Asp6^{APP-IP}, His218^{MMP-7}, His222^{MMP-7} and His228^{MMP-7} stably bind the zinc ion in the important catalytic site through the chelate interactions. Compared with APP-IP^{MMP-2} the N-terminal of APP-IP^{MMP-7} is upturned and unfavorable for the interaction with MMP-7 especially residues 178-182^{MMP-7} and residues 239-245^{MMP-7}, however, the C-terminal is suitable for the binding with the hydrophobic residues Tyr172^{MMP-7}, Ala184^{MMP-7}, Phe185^{MMP-7}, Ala186^{MMP-7} and Pro187^{MMP-7}. Figure 5 shows the binding pockets of N-terminal of APP-IP in MMP-7 and MMP-2.

As shown in Fig. 5 residues Pro238^{MMP-7} and Ile211^{MMP-7} are located at the top and bottom of APP-IP in MMP-7/APP-IP complex, respectively, and the distances between atom CB (Ile1^{APP-IP}) and atom CB (Ile211^{MMP-7}), and between atom CB (Ile1^{APP-IP}) and atom CB (Pro238^{MMP-7}) can represent the position of the N-terminal of APP-IP. We measured the distances mentioned above in MMP-7/APP-IP complex as well as the corresponding distances in MMP-2/APP-IP complex during 12 ns MD simulation (Fig. 6). The results show that Ile1^{APP-IP} moves far away from Ile211^{MMP-7} and close to P238^{MMP-7} after the 6.5 ns MD simulation in MMP-7/APP-IP complex, and the distances between CB (Ile1^{APP-IP}) and CB (Ile211^{MMP-7}) and between CB (Ile1^{APP-IP}) and CB (Pro238^{MMP-7}) stably maintain at about 20 and 6 Å to the end, respectively. However, both the corresponding distances in MMP-2/APP-IP complex hold a stable value of about 10 Å during the 12 ns MD simulation. The distance analysis proves that the binding mode of the APP-IP N-terminal in MMP-7/APP-IP complex is different from that in MMP-2/APP-IP complex. As discussed above, the energy decompose analysis also shows that the contributions of residues Ile1-Ser2-Tyr3^{APP-IP} in MMP-7/APP-IP complex are significantly different from those in MMP-2/APP-IP complex (see Fig. 3b).

In order to find out the causes leading to this difference between MMP-7/APP-IP and MMP-2/APP-IP complexes,

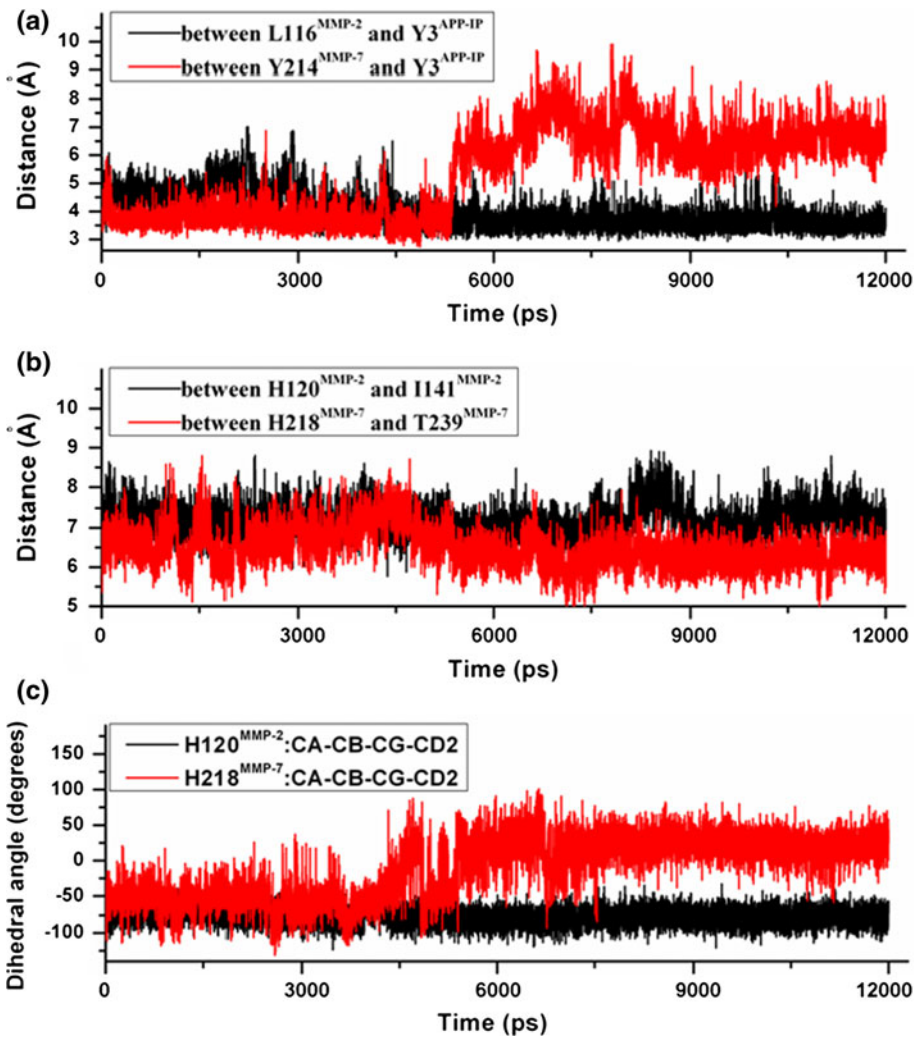

Fig. 7 The shortest distance between side chain of Tyr3^{APP-IP} and side chain of Tyr214^{MMP-7} (**a**), between side chain of His218^{MMP-7} and side chain of Thr239^{MMP-7} (**b**) in MMP-7/APP-IP system and the corresponding distance in MMP-2/APP-IP system during 12 ns MD simulation. **c** the dihedral angles of CA–CB–CG–CD2 in His218^{MMP-7} and His120^{MMP-2} during 12 ns MD simulation

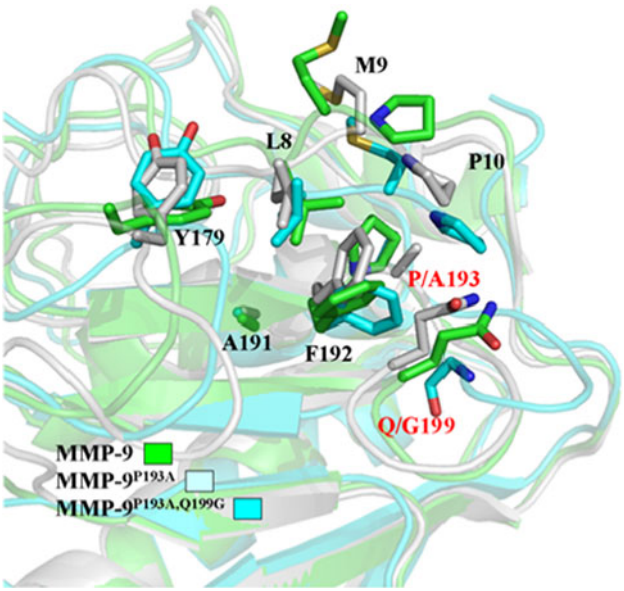

Fig. 8 The comparison of structure for the C-terminal of APP-IP between MMP-9/APP-IP and its two mutant complexes. All residues show the side chains in stick mode and hide the main chain except Gly199

we compared the binding pockets of the APP-IP N-terminal in MMP-7 and MMP-2 and found that Tyr214^{MMP-7} in the bottom of the pocket with a larger side chain than the corresponding residue Leu116^{MMP-2} makes the pocket in MMP-7 shallow (Fig. 5). Moreover, the shortest distance between His218^{MMP-7} and Thr239^{MMP-7}, which represents the size of the pocket, is smaller about 1 Å than that between His120^{MMP-2} and Ile141^{MMP-2} (Fig. 7b). The small and shallow binding pocket in MMP-7 makes the backbone of Tyr3^{APP-IP} in MMP-7 expose outside the pocket, while the backbone of Tyr3^{APP-IP} in MMP-2 bogs down in the pocket. Furthermore, to describe the different binding type of Tyr3^{APP-IP} in MMP-7 and MMP-2, the shortest distance between side chain of Tyr3^{APP-IP} and side chain of Tyr214^{MMP-7} and the corresponding distance in MMP-2/APP-IP complex during the 12 ns MD simulations were also calculated (Fig. 7a). It is shown that Tyr3^{APP-IP} moves far away from Tyr214^{MMP-7} after the 5 ns simulation in MMP-7/APP-IP, and the shortest distance maintains at about 7 Å, while the corresponding residues Tyr3^{APP-IP} and Leu116^{MMP-2} hold a stable distance at about 4 Å in MMP-2/APP-IP complex during the whole 12 ns MD simulation. The longer distance between Tyr3^{APP-IP} and Tyr214^{MMP-7} indicates that Tyr3^{APP-IP} could hardly enter into the pocket, but form van der Waals interaction with the external residue Pro238^{MMP-7} (see below). The change of the binding mode of Tyr3^{APP-IP} in MMP-7 leads to the dihedral angle formed by CA–CB–CG–CD2 of His218^{MMP-7} changing from −50° to 25° (Fig. 7c), and the π–π stacking interaction between Tyr3^{APP-IP} and His218^{MMP-7} also disappeared. Therefore, the unfavorable

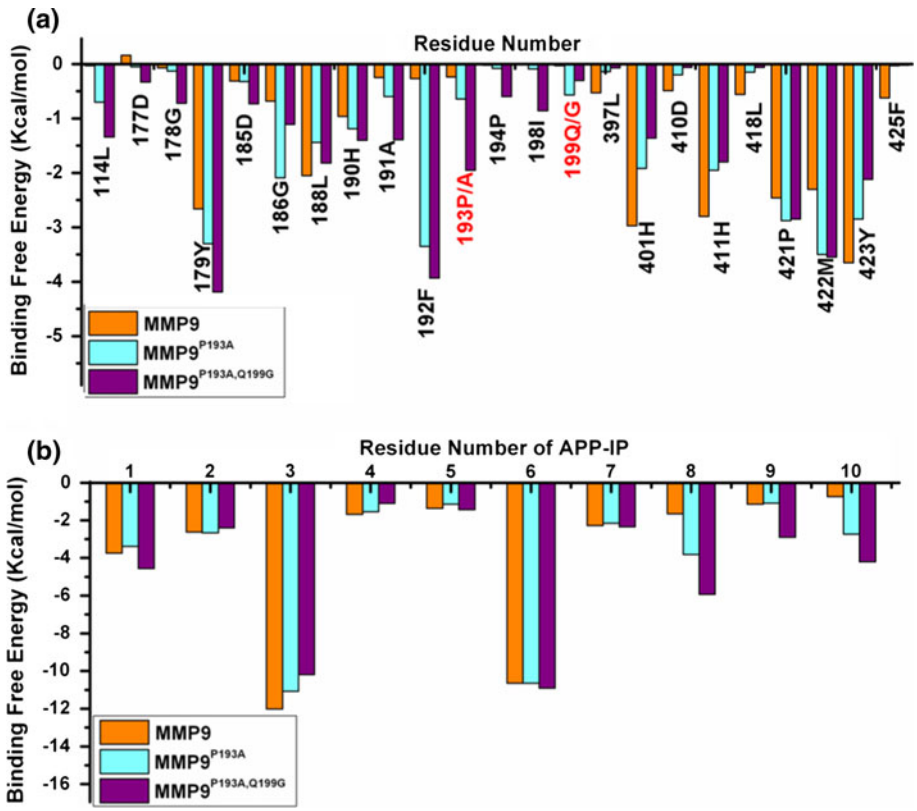

Fig. 9 The comparisons of key residues of MMP-9, MMP-9^{P193A}, MMP-9$^{P193A, Q199G}$ (**a**) and APP-IP (**b**) for MMP-9/APP-IP and its two mutant complexes

binding pocket of Tyr3^{APP-IP} in MMP-7 and the favorable van der Waals interaction of the external residue Pro238^{MMP-7} with Tyr3^{APP-IP} may cause the upturning of the N-terminal of APP-IP. To further verify the contribution of Tyr214 in MMP-7/APP-IP complex, the simulation of MMP-7^{Y214L}/APP-IP was carried out. The results indicate that the mutant gives a more favorable binding affinity −56.45 kcal/mol, which signifies that residue Tyr214 indeed affects the binding between MMP-7 and APP-IP (see the supporting information).

Compared MMP-7/APP-IP with MMP-2/APP-IP complex, it can be observed that there are mainly nine residues in MMP-7, Thr180, Leu181, Ala182, Ile210, Tyr214, Ala215, His218, Pro238 and Tyr240, showing distinct difference (Fig. 3a). Among these residues, the interaction between APP-IP and residues Thr180, Leu181, Ala182, Ile210, Tyr214, Ala215, His218 and Tyr240 of MMP-7/APP-IP complex (−0.32, −0.73, −0.61, −0.05, −0.06, −0.08, −1.15, −2.48 kcal/mol) are less favorable than those corresponding residues (−2.99, −3.17, −2.35, −1.33, −0.91, −1.04, −3.02, −4.29 kcal/mol) in MMP-2/APP-IP complex. However, the APP-IP interaction with residue Pro238 of MMP-7/APP-IP complex (−2.60 kcal/mol) is more favorable than the corresponding residue (−0.78 kcal/mol) in MMP-2/APP-IP complex, which just confirms our above analysis of the binding pocket of Tyr3^{APP-IP}. The N-terminal of APP-IP is far away from residues Thr180–Ala182^{MMP-7} and Ile210^{MMP-7}, resulting in the contributions of these residues decrease largely. Similarly, the distance between Tyr3^{APP-IP} and Tyr214^{MMP-7} is too large to form strong interaction. Compared with His120^{MMP-2}, the contribution of His218^{MMP-7} decreases by 1.87 kcal/mol, which is attributed to the disappearing of the π–π stacking interaction between Tyr3^{APP-IP} and His218^{MMP-7}.

Based on the above discussion, we would conclude that the different binding pockets of Tyr3^{APP-IP} in MMP-2 and MMP-7 lead to the large activity difference between MMP-2 and MMP-7.

MMP-9/APP-IP and its two mutant systems

The key residues of MMP-9/APP-IP, MMP-9^{P193A}/APP-IP and MMP-9$^{P193A,\ Q199G}$/APP-IP complexes are shown in Fig. 4d, e and f, respectively. Similarly, in these complexes, residues Asp6^{APP-IP}, His401^{MMP-9}, His405^{MMP-9} and His411^{MMP-9} stably bind the zinc ion in the important catalytic site through the chelate interactions. It is also shown that APP-IP binds MMP-9 or its mutants mainly at two distinct sites: the Ile1, Ser2 and Tyr3 of APP-IP nestle in a hydrophobic pocket of MMP-9, characterized by residues Phe425, Tyr423, Met422, Pro421, Ala189, Leu188, Leu187 and Gly186 (Fig. 4d), and another hydrophobic groove of MMP-9 formed by residues Leu114, Tyr179, Ala191, Phe192, Pro193 (Ala193 in the mutants), Pro194, Ile198, and Gln199 (Gly199 in the mutants) could accommodate residues Leu8, Met9 and Pro10 of the APP-IP.

Moreover, it can be found from Fig. 3a that residues Tyr179, Leu187, His401, Met422 and Tyr423 in MMP-9 have large contributions to the binding free energy, similar to the corresponding residues in MMP-2, which indicate that these residues are not the reason for the inhibitor selectivity. However, the seven residues of MMP-9, Ala189, His190, Ala191, Phe192, Pro193, His411 and Pro421, show distinct differences (Fig. 3a). Among these seven residues, the interaction between APP-IP and residues Ala189, His190, Ala191, Phe192, and Pro193 of MMP-9 complex (−0.68, −0.96, −0.25, −0.27, −0.24 kcal/mol) are less favorable than those corresponding residues (−2.35, −2.80, −2.42, −4.38, −1.78 kcal/mol) in MMP-2/APP-IP complex, while the APP-IP interaction with residues His411 and Pro421 of MMP-9 complex (−2.80, −2.46 kcal/mol) are more favorable than that with the corresponding residues (−1.27, −0.78 kcal/mol) in MMP-2/APP-IP complex. The results indicate that the interaction of APP-IP C-terminal with MMP-9 plays an important role in the decrease of the binding affinity in MMP-9/APP-IP complex.

Compared with MMP-2/APP-IP, the side chains of residues Pro193^{MMP-9} and Gln199^{MMP-9} in MMP-9/APP-IP are larger than those of the corresponding residues Ala87^{MMP-2} and Gly93^{MMP-2}, and the bulky side chains block the C-terminal residues Leu8, Met9 and Pro10 of APP-IP to be close to residues 189-193^{MMP-9} and make the contribution of 189-193^{MMP-9} be smaller than that of the corresponding residues in MMP-2 (see Figs. 3, 4d). The reason why the C-terminal of APP-IP is unfavorable when binding with MMP-9 can be further explained clearly in the two mutations on Pro193^{MMP-9} and Gln199^{MMP-9}.

As mentioned above, after the single (P193A) and double (P193A, Q199G) mutations, the C-terminal of APP-IP moves closer to MMP-9 (see Figs. 4a, 8), and the binding free energies decrease by about 4 and 16 kcal/mol, respectively. Figure 9 gives the comparison of the key residues of APP-IP and MMP-9, MMP-9^{P193A} and MMP-9$^{P193A,\ Q199G}$ for MMP-9/APP-IP, MMP-9^{P193A}/APP-IP and MMP-9$^{P193A,\ Q199G}$/APP-IP complexes. Compared with MMP-9/APP-IP complex, it is notable that the contributions of residues Leu114^{MMP-9}, Tyr179^{MMP-9}, Ala191^{MMP-9}, Phe192^{MMP-9} and Pro193^{MMP-9} (Ala193^{MMP-9} in the mutants) remarkably increase to −0.7, −3.3, −0.6, −3.35 and −0.64 kcal/mol in the single mutant and to −1.34, −4.19, −1.39, −3.93 and −1.95 kcal/mol in the double mutant, respectively, which is attributed to the contribution of the van der Waals. The increase contributions of these residues are corresponding to the decrease of the binding free energies of Leu8, Met9 and Pro10 in APP-IP in both mutants

Table 2 Percentage of hydrogen bonds related to $Leu8^{APP-IP}$ during the 12 ns MD simulations of MMP-2/APP-IP, MMP-9/APP-IP and the two mutant complexes

Complexes	Donor	Acceptor	Occupied (%)	Distance (Å)	Angle (deg)[a]
MMP-2/APP-IP	:85@O	:8@H-:8@N(APP-IP)	56.40	3.219	156.15
MMP-9/APP-IP	:191@O	:8@H-:8@N(APP-IP)	–	–	–
$MMP\text{-}9^{P193A}$/APP-IP	:191@O	:8@H-:8@N(APP-IP)	–	–	–
$MMP\text{-}9^{P193A,Q199G}$/APP-IP	:191@O	:8@H-:8@N(APP-IP)	32.45	3.257	152.12
MMP-14/APP-IP	:202@O	:8@H-:8@N(APP-IP)	28.20	3.319	148.35
MMP-2/APP-IP	:8@O(APP-IP)	:87@H-:87@N	100.00	2.899	163.31
MMP-9/APP-IP	:8@O(APP-IP)	:193@H-:193@N	–	–	–
$MMP\text{-}9^{P193A}$/APP-IP	:8@O(APP-IP)	:193@H-:193@N	–	–	–
$MMP\text{-}9^{P193A,Q199G}$/APP-IP	:8@O(APP-IP)	:193@H-:193@N	97.90	2.998	161.25
MMP-14/APP-IP	:8@O(APP-IP)	:204@H-:204@N	77.40	3.188	160.83

[a] The angles listed in Table 2 are the real hydrogen bond angles rather than the stored angles (the supplementary angles of the real hydrogen bond angles) obtained from the *ptraj* program of AMBER. "–"represents no hydrogen bond was found

(see Fig. 9b), which indicate that the mutations are favorable for the interaction between the C-terminal of APP-IP and MMP-9. The contributions of residues His401, His411 and Tyr423 decrease slightly in the single and double mutations. However, the total contribution is increased as shown in Table 1. We can summarize that the difference of the binding affinities among MMP-9/APP-IP and its two mutant complexes is mainly derived from the contribution of the van der Waals energies.

Figures 4a, 8, and 9b show the difference of the C-terminal of APP-IP between MMP-2/APP-IP and MMP-9/APP-IP. To understand the detailed interaction mechanism of C-terminal of APP-IP with MMP-2, MMP-9 and the two mutants, we investigated the hydrogen bond network related to C-terminal of APP-IP in the four complexes. From the crystal structure analysis [22], there exist two hydrogen bonds between $Leu8^{APP-IP}$ and $Ala85^{MMP-2}$ and between $Leu8^{APP-IP}$ and $Ala87^{MMP-2}$ in MMP-2/APP-IP complex, therefore the hydrogen bond information related to $Leu8^{APP-IP}$ was explored here. In the hydrogen bond calculation, if the donor–acceptor (H) distance is smaller than 3.5 Å and the donor–acceptor (H)-acceptor angle is larger than 120°, a hydrogen bond is defined. The visible percentages of MMP2/APP-IP and MMP-9/APP-IP complexes during the MD simulations, as well as the distances between the two pairs of atoms probably forming hydrogen bonds, were calculated, and the results were shown in Table 2 and Fig. 10, respectively.

As shown in Fig. 10 and Table 2, the distances of the two pairs of atoms, between atom O ($Ala85^{MMP-2}$) and atom N ($Leu8^{APP-IP}$) and between atom N ($Ala87^{MMP-2}$) and atom O ($Leu8^{APP-IP}$), fluctuate around 3.0 Å during the 12 ns MD simulation in MMP-2/APP-IP complex, and the hydrogen bond occupancies are 56.40 and 100 %, respectively, which is consistent with the experimental data (Table 2). In the double mutant both the distances of the two pairs of atoms, between atom O ($Ala191^{MMP-9}$) and atom N ($Leu8^{APP-IP}$) and between atom N ($Ala193^{MMP-9}$) and atom O ($Leu8^{APP-IP}$), fluctuate around 3.0 Å during the last 4.5 ns MD simulation, and the hydrogen bond occupancies are 32.45 % and 97.90 %, respectively (see Table 2). Clearly, the mutation at residues P193A and Q199G of MMP-9 leads to form two new hydrogen bonds, making the C-terminal of APP-IP bind MMP-9 tighter. However, the distances of the corresponding two pairs of atoms are so far that could hardly form stable hydrogen bonds in the WT and single mutant complexes. The missing hydrogen bonds in MMP-9/APP-IP and $MMP\text{-}9^{P193A}$/APP-IP complexes should be one of the reasons leading to the smaller binding affinities of the APP-IP C-terminal with MMP-9 and the single mutant than with MMP-2 and the double mutant.

Our calculations demonstrate that the poor selectivity of APP-IP toward MMP-9 is mainly related with the weakening of the interaction between the APP-IP C-terminal and the binding pocket formed by residues Leu114, Tyr179, Ala191, Phe192, Pro193, Pro194, Ile198, and Gln199 in MMP-9 due to the bulky side chains of Pro193 and Gln199. The mutations at residues P193A and Q199G of MMP-9 actually changed the binding modes between MMP-9 and APP-IP, especially the C-terminal of APP-IP, through stronger van der Waals contribution of Tyr179, Ala191, Phe192 and Ala193 and new formed H-bond interaction in the double mutant.

MMP-14/APP-IP system

Like other MMPs, residue $Asp6^{APP-IP}$ and residues $His239^{MMP-14}$, $His243^{MMP-14}$, $His249^{MMP-14}$ in MMP-14/APP-IP complex bind the zinc ion through chelation.

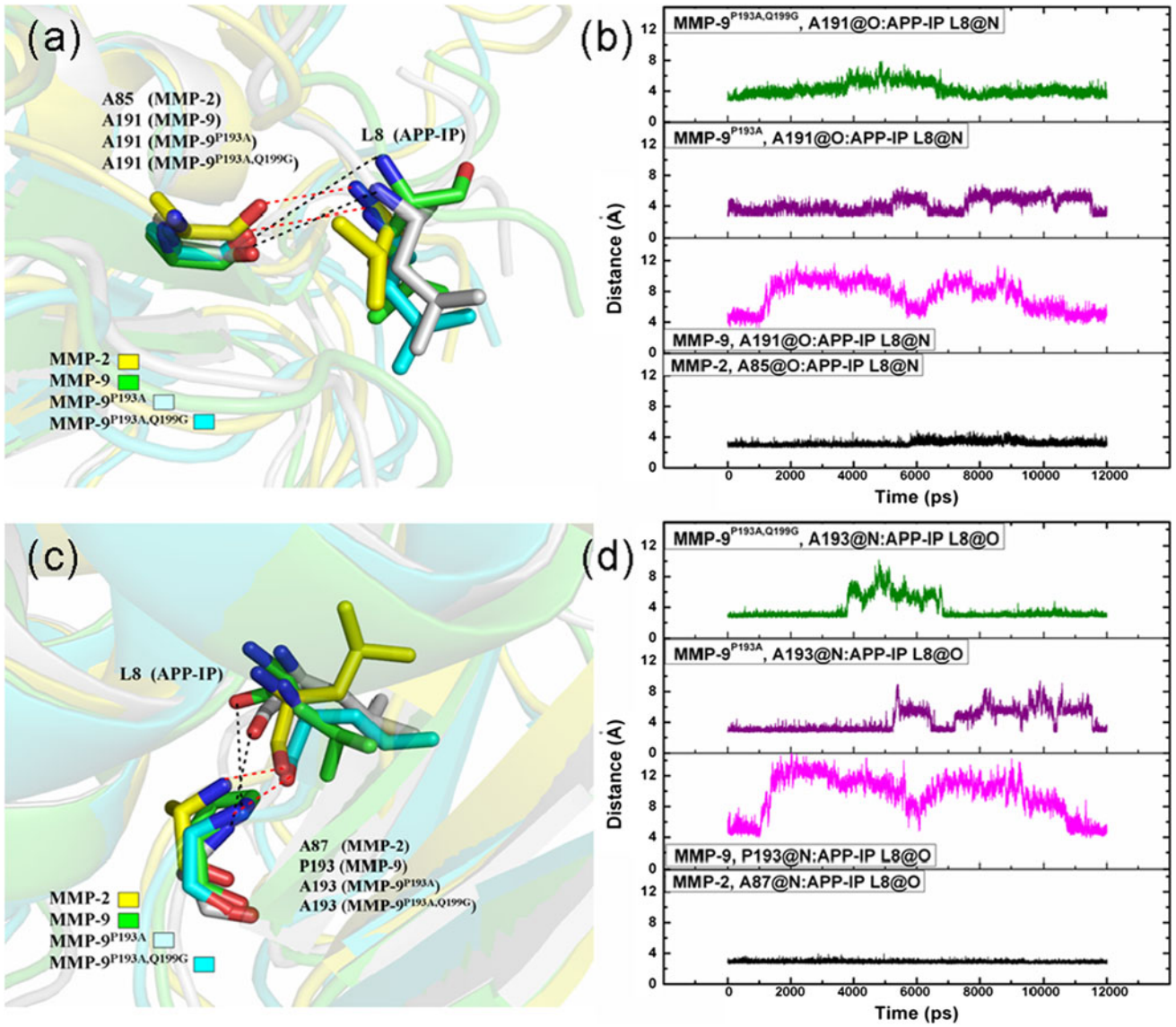

Fig. 10 The distances between atom O (Ala85$^{\text{MMP-2}}$/Ala191$^{\text{MMP-9}}$/Ala191$^{\text{MMP-9-P193A}}$/Ala191$^{\text{MMP-9–P193A, Q199G}}$) and N (Leu8$^{\text{APP-IP}}$) are shown in **a** and **b**. The distance between atom N (Ala87$^{\text{MMP-2}}$/Pro193$^{\text{MMP-9}}$/Ala193$^{\text{MMP-9–P193A}}$/Ala193$^{\text{MMP-9–P193A, Q199G}}$) and O (Leu8$^{\text{APP-IP}}$) are shown in **c** and **d** during the 12 ns MD simulations

Although the contribution of Asp6$^{\text{APP-IP}}$ is decreased compared with that in the other complexes, Asp6$^{\text{APP-IP}}$ still has a strong interaction with MMP-14. As discussed above, it seems that both the N and C terminals of APP-IP are suitable for MMP-14 interacting, with residues Leu117, Leu199-Phe204, Ile209, Asn229, Val236, His239, Glu240, His243, His249, and Pro259-Tyr261. The experimental data really shows that APP-IP has a worse activity against MMP-14 than MMP-2 [20]. To find out the key residues associated with the different binding affinities between MMP-2/APP-IP and MMP-14/APP-IP, the meticulous comparison of binding mode of the two complexes is carried out and shown in Fig. 11. It shows that Leu8$^{\text{APP-IP}}$ and Tyr3$^{\text{APP-IP}}$ have a fixed binding conformation in both complexes due to the two hydrogen bonds for Leu8$^{\text{APP-IP}}$ (see Table 2) and the deep hydrophobic pocket for Tyr3-$^{\text{APP-IP}}$. Meanwhile, the larger side chain of Phe204$^{\text{MMP-14}}$ than Ala87$^{\text{MMP-2}}$ would repulse Ala7$^{\text{APP-IP}}$ in MMP-14/APP-IP through larger steric effect which can be observed from Fig. 11 directly. The Ala7$^{\text{APP-IP}}$ in MMP-14/APP-IP moves closer to Thr190$^{\text{MMP-14}}$ and the main chain of Asp6$^{\text{APP-IP}}$ is closer to Tyr3$^{\text{APP-IP}}$ in MMP-14/APP-IP. Therefore, the region of residues Asp6$^{\text{APP-IP}}$, Asn5$^{\text{APP-IP}}$ and Gly4$^{\text{APP-IP}}$ is ridgy in MMP-14/APP-IP complex.

As shown in Fig. 3, compared with MMP-2/APP-IP, it can be found that there are mainly nine residues of MMP-

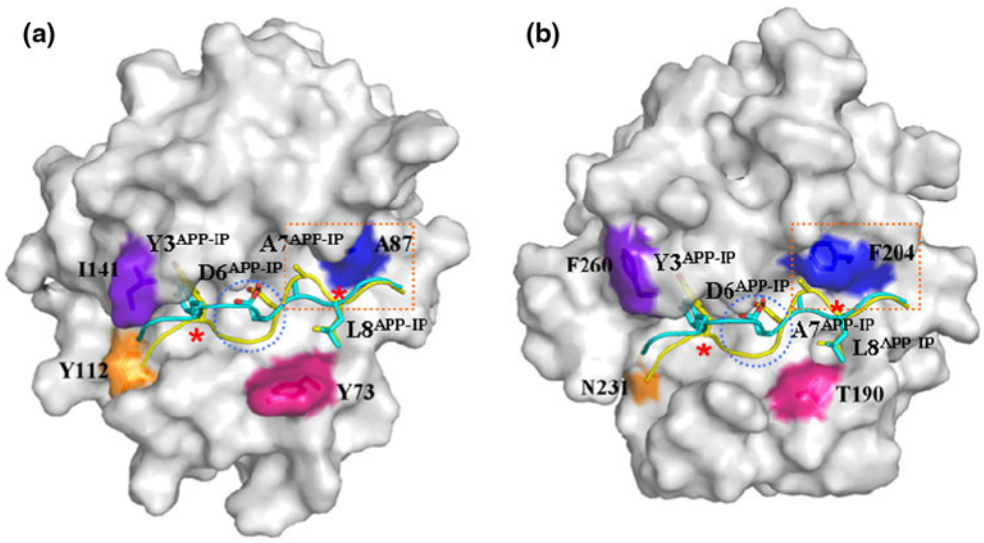

Fig. 11 Molecular surface of MMP-2 (**a**) and MMP-14 (**b**) with APP-IP^{MMP-2} (in *yellow*) and APP-IP^{MMP-14} (in *cyan*). Four important and different residues in MMPs are colored

14, Thr190, Phe198, Leu199, Ala200, Phe204, Asn231, Pro259, Phe260 and Tyr261, showing distinct differences. Among which, the interactions between APP-IP and the six residues Thr190, Phe198, Leu199, Ala200, Asn231 and Tyr261 of MMP-14/APP-IP complex (−0.75, −0.57, −1.34, −0.72, −0.14 and −2.46 kcal/mol) are less favorable than those corresponding residues (−2.71, −2.99, −3.17, −2.35, −1.33 and −4.29 kcal/mol) in MMP-2/APP-IP complex. However, the APP-IP interaction with the three residues Phe204, Pro259 and Phe260 of MMP-14/APP-IP complex (−4.31, −2.83 and −3.24 kcal/mol) are more favorable than those corresponding residues (−1.78, −0.78 and −1.94 kcal/mol) in MMP-2/APP-IP complex.

The smaller contribution of Thr190^{MMP-14} and Asn231^{MMP-14} than the corresponding residues Tyr73^{MMP-2} and Tyr112^{MMP-2} is attributed to their weaker van der Waals interaction with the hydrophobic residues Leu8^{APP-IP} and Ile1^{APP-IP}, respectively (see Fig. 12). As stated above, the position of residues Asn7-Gly4^{APP-IP} in MMP-14/APP-IP complex is different from that in MMP-2/APP-IP complex, which makes the contributions of residues Gly196–Ala202^{MMP-14}, especially Phe198^{MMP-14}, decrease largely, compared with the MMP-2/APP-IP complex. Whereas residues Phe204^{MMP-14} and Phe260^{MMP-14} with larger aromatic rings can contribute stronger hydrophobic interactions than Ala87^{MMP-2} and Ile141^{MMP-2}, so they are more favorable for APP-IP binding.

Compared all complexes we studied, residue Tyr214^{MMP-7} in MMP-7/APP -IP complex, which is different from the corresponding residues (Leu116^{MMP-2}, Leu397^{MMP-9} and Leu235^{MMP-14}) in other complexes, makes the binding pocket of the N-terminal of APP-IP in MMP-7 be different from that in MMP-2, MMP-9 and MMP-14, leading to the significant diverse binding modes. Similarly, residues Pro193^{MMP-9} and Gln199 $^{MMP-9}$ in MMP-9/APP-IP complex are different from the corresponding residues in other systems, which make the C-terminal of APP-IP^{MMP-9} unfavorable for MMP-9 binding. Furthermore, compared MMP-14/APP-IP and MMP-9/APP-IP, the larger volume Phe204^{MMP-14} has a more favorable energy contribution than Pro193^{MMP-9}, though they locate at the same regions in the structures and both are non-polar amino acid. The contribution difference between Phe204^{MMP-14} and Pro193^{MMP-9} is attributed to the special space position of the side chain of Phe204^{MMP-14}. The free rotation bonds of the CA–CB and CB–CG in Phe204^{MMP-14} make the side chain phenyl could take an advantaged position for the APP-IP interacting. Moreover, the phenyl side chain of Phe204^{MMP-14} responses to its

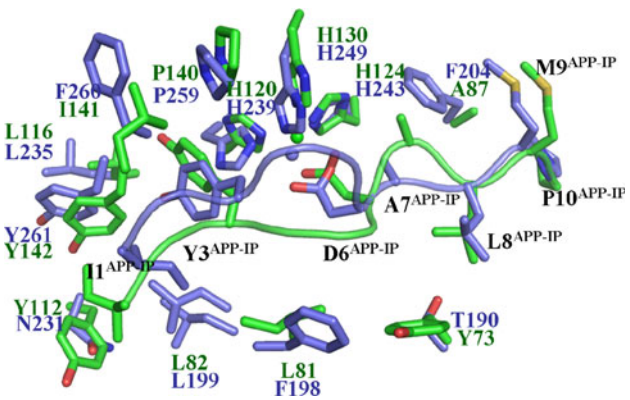

Fig. 12 The comparison of the structure between MMP-14/APP-IP and MMP-2/APP-IP. (MMP-14/APP-IP complex is colored in *blue* and MMP-2/APP-IP complex in *green*, all residues are shown in stick model.)

strong van der Waals contribution by interacting with $Met9^{APP-IP}$ and $Ala7^{APP-IP}$.

Conclusions

In this study, to clarify the selectivity and mechanism of APP-IP toward MMP-2, MMP-7, MMP-9, and MMP-14 MD simulations, MM/GBSA free energy calculations, and MM/GBSA free energy decomposition analysis were conducted. The calculated results show that the predicted binding free energy of MMP-2/APP-IP complex is more favorable than that of the MMP-7/APP-IP, MMP-9/APP-IP, MMP-14/APP-IP complexes, which is in accordance with the experimental data. It is also observed that the van der Waals contribution is more crucial than other energy terms' contribution for distinguishing the binding affinities among the four complexes.

Compared with MMP-2/APP-IP complex, the $Tyr214^{MMP-7}$ with a larger side chain than the corresponding residue $Leu116^{MMP-2}$ makes the binding pocket of $Tyr3^{APP-IP}$ in MMP-7 smaller than that in MMP-2 leading to the N-terminal of APP-IP unfavorable for MMP-7 binding and the large activity difference. For the MMP-9/APP-IP complex, the C-terminal of APP-IP is unfavorable for MMP-9 binding due to the steric effect of $Pro193^{MMP-9}$ and $Gln199^{MMP-9}$. The mutations P193A and Q199G in MMP-9 alternate the binding pattern of APP-IP especially in the C-terminal by forming two new hydrogen bonds and hydrophobic interaction between the inhibitor and MMP-9, and largely promote the binding ability of MMP-9, which is also in good agreement with the experimental data, however, the binding affinity is still weaker than that of MMP-2. For MMP-14/APP-IP complex, the larger volume residue $Phe204^{MMP-14}$ than $Ala87^{MMP-2}$ with steric effect influences the position of $Ala7^{APP-IP}$, and further causes the displacement of residues $Asp6^{APP-IP}$, $Asn5^{APP-IP}$ and $Gly4^{APP-IP}$, which may be one of the causes associated with activity. In addition, another reason affecting the binding affinity should be the unfavorable polar residues Asn231 and Thr190 in MMP-14.

In Summary, it is feasible to investigate the selectivity of APP-IP toward MMPs by using the combination of different molecular modeling techniques. We hope this work would provide valuable structural information to understand the unspecific binding between APP-IP and MMPs except MMP-2. Based on these findings, the peptide sequences that are highly selective to MMP-7, MMP-9 and MMP-14, respectively, will be studied in the future.

Acknowledgments We gratefully acknowledge the National Natural Science Foundation of China (No. 21173264) and the Foundation of Knowledge Innovative Engineering of Chinese Academy of Sciences (No. ZNWH-2011-011) for supporting this work.

References

1. Hooper NM (1996) Zinc metalloproteases in health and disease. Taylor, Francis
2. Docherty AJP, O'Connell J, Crabbe T, Angal S, Murphy G (1992) The matrix metalloproteinases and their natural inhibitors: prospects for treating degenerative tissue diseases. Trends Biotechnol 10:200–207
3. Matrisian LM (1992) The matrix-degrading metalloproteinases. BioEssays 14(7):455–463
4. Stetler-Stevenson WG, Aznavoorian S, Liotta LA (1993) Tumor cell interactions with the extracellular matrix during invasion and metastasis. Annu Rev Cell Biol 9(1):541–573
5. Liotta LA (1986) Tumor invasion and metastases—role of the extracellular matrix: Rhoads memorial award lecture. Cancer Res 46(1):1–7
6. Collier IE, Wilhelm SM, Eisen AZ, Marmer BL, Grant GA, Seltzer JL, Kronberger A, He CS, Bauer EA, Goldberg GI (1988) H-Ras oncogene-transformed human bronchial epithelial cells (TBE-1) secrete a single metalloprotease capable of degrading basement membrane collagen. J Biol Chem 263(14): 6579–6587
7. Wilhelm SM, Collier IE, Marmer BL, Eisen AZ, Grant GA, Goldberg GI (1989) SV40-transformed human lung fibroblasts secrete a 92-kDa type IV collagenase which is identical to that secreted by normal human macrophages. J Biol Chem 264(29):17213–17221
8. Van Wart HE, Birkedal-Hansen H (1990) The cysteine switch: a principle of regulation of metalloproteinase activity with potential applicability to the entire matrix metalloproteinase gene family. Proc Natl Acad Sci 87(14):5578–5582
9. Becker JW, Marcy AI, Rokosz LL, Axel MG, Burbaum JJ, Fitzgerald PMD, Cameron PM, Esser CK, Hagmann WK, Hermes JD, Springer JP (1995) Stromelysin-1: three-dimensional structure of the inhibited catalytic domain and of the C-truncated proenzyme. Protein Sci 4(10):1966–1976
10. Bode W, Gomis-Rüth F-X, Stöckler W (1993) Astacins, serralysins, snake venom and matrix metalloproteinases exhibit identical zinc-binding environments (HEXXHXXGXXH and Met-turn) and topologies and should be grouped into a common family, the 'metzincins'. FEBS Lett 331(1–2):134–140
11. Gomis-Rüth FX, Gohlke U, Betz M, Knäuper V, Murphy G, López-Otín C, Bode W (1996) The helping hand of collagenase-3 (MMP-13): 2.7 Å crystal structure of its C-terminal haemopexin-like domain. J Mol Biol 264(3):556–566
12. Brew K, Dinakarpandian D, Nagase H (2000) Tissue inhibitors of metalloproteinases: evolution, structure and function. Biochim Biophys Acta 1477(1–2):267–283
13. Amour A, Slocombe PM, Webster A, Butler M, Knight CG, Smith BJ, Stephens PE, Shelley C, Hutton M, Knauper V, Docherty AJ, Murphy G (1998) TNF-alpha converting enzyme (TACE) is inhibited by TIMP-3. FEBS Lett 435(1):39–44
14. Amour A, Knight CG, Webster A, Slocombe PM, Stephens PE, Knäuper V, Docherty AJP, Murphy G (2000) The in vitro activity of ADAM-10 is inhibited by TIMP-1 and TIMP-3. FEBS Lett 473(3):275–279
15. Kashiwagi M, Tortorella M, Nagase H, Brew K (2001) TIMP-3 is a potent inhibitor of aggrecanase 1 (ADAM-TS4) and aggrecanase 2 (ADAM-TS5). J Biol Chem 276(16):12501–12504
16. Betz M, Huxley P, Davies SJ, Mushtaq Y, Pieper M, Tschesche H, Bode W, Gomis-Ruth FX (1997) 1.8-A crystal structure of the catalytic domain of human neutrophil collagenase (matrix metalloproteinase-8) complexed with a peptidomimetic hydroxamate primed-side inhibitor with a distinct selectivity profile. Eur J Biochem 247(1):356–363

17. Brandstetter H, Grams F, Glitz D, Lang A, Huber R, Bode W, Krell HW, Engh RA (2001) 1.8-A crystal structure of a matrix metalloproteinase 8-barbiturate inhibitor complex reveals a previously unobserved mechanism for collagenase substrate recognition. J Biol Chem 276(20):17405–17412
18. Jia MC, Schwartz MA, Sang QA (2000) Suppression of human microvascular endothelial cell invasion and morphogenesis with synthetic matrixin inhibitors. Targeting angiogenesis with MMP inhibitors. Adv Exp Med Biol 476:181–194
19. Finzel BC, Baldwin ET, Bryant GL Jr, Hess GF, Wilks JW, Trepod CM, Mott JE, Marshall VP, Petzold GL, Poorman RA, O'Sullivan TJ, Schostarez HJ, Mitchell MA (1998) Structural characterizations of nonpeptidic thiadiazole inhibitors of matrix metalloproteinases reveal the basis for stromelysin selectivity. Protein Sci 7(10):2118–2126
20. Higashi S, Miyazaki K (2003) Identification of a region of beta-amyloid precursor protein essential for its gelatinase A inhibitory activity. J Biol Chem 278(16):14020–14028
21. Higashi S, Miyazaki K (2008) Identification of amino acid residues of the matrix metalloproteinase-2 essential for its selective inhibition by beta-amyloid precursor protein-derived inhibitor. J Biol Chem 283(15):10068–10078
22. Hashimoto H, Takeuchi T, Komatsu K, Miyazaki K, Sato M, Higashi S (2011) Structural basis for matrix metalloproteinase-2 (MMP-2)-selective inhibitory action of β-amyloid precursor protein-derived inhibitor. J Biol Chem 286(38):33236–33243
23. Gohlke H, Case DA (2004) Converging free energy estimates: MM-PB(GB)SA studies on the protein–protein complex Ras-Raf. J Comput Chem 25(2):238–250
24. Hou T, McLaughlin W, Lu B, Chen K, Wang W (2005) Prediction of binding affinities between the human amphiphysin-1 SH3 domain and its peptide ligands using homology modeling, molecular dynamics and molecular field analysis. J Proteome Res 5(1):32–43
25. Hou T, Zhang W, Case DA, Wang W (2008) Characterization of domain–peptide interaction interface: a case study on the amphiphysin-1 SH3 domain. J Mol Biol 376(4):1201–1214
26. Fang L, Zhang H, Cui W, Ji M (2008) Studies of the mechanism of selectivity of protein tyrosine phosphatase 1B (PTP1B) bidentate inhibitors using molecular dynamics simulations and free energy calculations. J Chem Inf Model 48(10):2030–2041
27. Larkin MA, Blackshields G, Brown NP, Chenna R, McGettigan PA, McWilliam H, Valentin F, Wallace IM, Wilm A, Lopez R, Thompson JD, Gibson TJ, Higgins DG (2007) Clustal W and Clustal X version 2.0. Bioinformatics 23(21):2947–2948
28. Berman HM, Westbrook J, Feng Z, Gilliland G, Bhat TN, Weissig H, Shindyalov IN, Bourne PE (2000) The protein data bank. Nucleic Acids Res 28(1):235–242
29. Browner MF, Smith WW, Castelhano AL (1995) Crystal structures of matrilysin-inhibitor complexes. Biochemistry 34(20):6602–6610
30. Rowsell S, Hawtin P, Minshull CA, Jepson H, Brockbank SM, Barratt DG, Slater AM, McPheat WL, Waterson D, Henney AM, Pauptit RA (2002) Crystal structure of human MMP9 in complex with a reverse hydroxamate inhibitor. J Mol Biol 319(1):173–181
31. Fernandez-Catalan C, Bode W, Huber R, Turk D, Calvete JJ, Lichte A, Tschesche H, Maskos K (1998) Crystal structure of the complex formed by the membrane type 1-matrix metalloproteinase with the tissue inhibitor of metalloproteinases-2, the soluble progelatinase A receptor. EMBO J 17(17):5238–5248
32. Jorgensen WL, Chandrasekhar J, Madura JD, Impey RW, Klein ML (1983) Comparison of simple potential functions for simulating liquid water. J Chem Phys 79(2):926–935
33. Case DA, Cheatham TE, Darden T, Gohlke H, Luo R, Merz KM Jr, Onufriev A, Simmerling C, Wang B, Woods RJ (2005) The Amber biomolecular simulation programs. J Comput Chem 26(16):1668–1688
34. Duan Y, Wu C, Chowdhury S, Lee MC, Xiong G, Zhang W, Yang R, Cieplak P, Luo R, Lee T, Caldwell J, Wang J, Kollman P (2003) A point-charge force field for molecular mechanics simulations of proteins based on condensed-phase quantum mechanical calculations. J Comput Chem 24(16):1999–2012
35. Stote RH, Karplus M (1995) Zinc binding in proteins and solution: a simple but accurate nonbonded representation. Proteins Struct Funct Bioinform 23(1):12–31
36. Ryckaert J-P, Ciccotti G, Berendsen HJC (1977) Numerical integration of the cartesian equations of motion of a system with constraints: molecular dynamics of n-alkanes. J Comput Phys 23(3):327–341
37. Darden T, York D, Pedersen L (1993) Particle mesh Ewald: an N [center-dot] log(N) method for Ewald sums in large systems. J Chem Phys 98(12):10089–10092
38. Kollman PA, Massova I, Reyes C, Kuhn B, Huo S, Chong L, Lee M, Lee T, Duan Y, Wang W, Donini O, Cieplak P, Srinivasan J, Case DA, Cheatham TE (2000) Calculating structures and free energies of complex molecules: combining molecular mechanics and continuum models. Acc Chem Res 33(12):889–897
39. Tsui V, Case DA (2000) Theory and applications of the generalized Born solvation model in macromolecular simulations. Biopolymers 56(4):275–291
40. Weiser J, Shenkin PS, Still WC (1999) Approximate atomic surfaces from linear combinations of pairwise overlaps (LCPO). J Comput Chem 20(2):217–230
41. Gohlke H, Kiel C, Case DA (2003) Insights into protein–protein binding by binding free energy calculation and free energy decomposition for the Ras–Raf and Ras–RalGDS complexes. J Mol Biol 330(4):891–913
42. Onufriev A, Bashford D, Case DA (2004) Exploring protein native states and large-scale conformational changes with a modified generalized born model. Proteins Struct Funct Bioinform 55(2):383–394
43. Delano WL (2002) The PyMOL molecular graphics system on World Wide Web http://www.pymol.org